THE JOURNAL OF PHYSICAL CHEMISTRY C

Article

pubs.acs.org/JPCC

Gas Adsorption Thermodynamics Deduced from the Electrical Responses in Gas-Gated Field-Effect Nanosensors

Baiyi Zu,[†] Bin Lu,[†] Zheng Yang,[†,‡] Yanan Guo,[†] Xincun Dou,*[,†] and Tao Xu*[,§]

[†]Laboratory of Environmental Science and Technology, The Xinjiang Technical Institute of Physics & Chemistry; Key Laboratory of Functional Materials and Devices for Special Environments, Chinese Academy of Sciences, Urumqi 830011, China

[‡]University of Chinese Academy of Sciences, Beijing 100049, China

[§]Department of Chemistry and Biochemistry, Northern Illinois University, DeKalb, Illinois 60115, United States

Supporting Information

ABSTRACT: Understanding the underlying physical chemistry governing the nanomaterial-based electrical gas sensing process is pivotal for the rational design of high-performance gas sensors. Herein, using a remarkable ppb-level NO_2-gated field-effect nanosensor that is based on a reduced graphene oxide rGO/TiO_2 nanoparticle heterojunction, as an exploratory platform, we have established a generic physical chemistry model to quantitatively gain insight into the correlation between the measured source-drain (S-D) current and the gas sorption thermodynamics in this NO_2 nanosensor. Based on thin-film field-effect transistor theory, the measured S-D current leads to the solution to the gas-induced gate voltage, which further solves the surface charge density using the Graham surface potential vs surface charge density function. Consequently, based on the Van't Hoff equation, key thermodynamic information can be obtained from this model including adsorption equilibrium constants and adsorption enthalpy of NO_2 on TiO_2 nanoparticles. The acquisition of gas adsorption enthalpy provides a generic and nonspecific method to identify the nature of the adsorbed molecules.

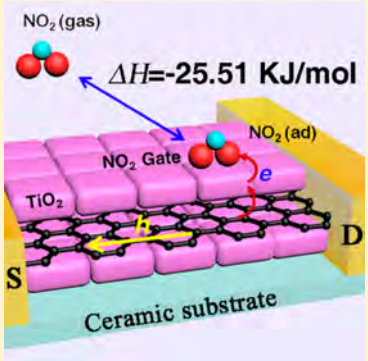

INTRODUCTION

The exploration of nanosensors for highly sensitive and selective detection of chemical species is an appealing topic in nanoscience.[1−10] For example, semiconductor nanomaterial-based biological field-effect sensors, in which the gate voltage is modulated by biological molecules of interest and results in depletion or accumulation of carriers within the sensor structure, has been a very active branch of nanosensors.[1] The field-effect sensors are also widely used in chemical industries for detection of toxic environmental pollutants and early alarming of hazardous and explosive gas leaks.[8,11−15] In particular, due to the increasing combustion exhausts from automobiles and thermal power plants, there is a pressing need on the high performance detection of NO_2 at ppb (parts per billion) level for early alarming,[16] as NO_2 is confirmed to be highly harmful to human health and the environment in formats of acid rain, etc.[17] The exposure time for human beings in NO_2 is suggested to be limited to no more than 8 h in even 3 ppm (parts per million) NO_2.[18]

Nonetheless, current attempts on exploring nanomaterial-based gas sensors for ppm or sub-ppm level NO_2 detection mainly focus on the incremental improvement on the sensor performance.[16,19−22] In contrast, there is a serious lack of fundamental understanding and quantitative analysis on the underlying sensing mechanism that governs the correlation between the NO_2 sorption thermodynamics and the response of the electric signal generated in the sensing elements. Such unbalance effort limits the theoretic basis for the designing of high performance NO_2 sensors. Therefore, in this work, besides developing ppb-level NO_2-gated nanosensors, we also strive to establish an analytic model to correlate the gas sorption equilibrium and the consequent gate voltage effect on the source-drain current in the sensing element based on fundamental thermodynamics, surface charge function, and field-effect transistor (FET) theory.

Typical NO_2 sensing elements include nanostructured semiconducting metal oxides, carbon nanotubes, and graphene,[16,19,22−33] of which graphene and its chemically modified derivatives, e.g., graphene oxide (GO) and reduced graphene oxide (rGO), have attracted extensive attention for their high electron mobility (15000 $cm^2\ V^{-1}\ s^{-1}$ for graphene, for example).[16,34] The single atomic layer thickness that is highly sensitive to the electronic perturbations from the adsorbed gas molecules within its proximity[19] as well as the high surface area (theoretically 2600 m^2g^{-1}) accommodates sufficient reactive sites for the nucleation[35−38] and growth of polarizable gas docking centers, such as SnO_2 nanoparticles on it.[16] Although various graphene-based gas sensors or nanoparticle/graphene composites,[30,32] especially SnO_2/rGO-based gas sensors, have been fabricated into gas sensors in the past several years,[16,19−21] the current efforts only address the electrical response to the gas concentrations, while no quantitative relationship between

Received: May 29, 2014
Revised: June 6, 2014
Published: June 11, 2014

the sensing current and the gas absorption themodynamics has been established.

As shown in Figure 1, herein, we designed and constructed an rGO/TiO_2 heterojunction NO_2 sensor, in which both sides

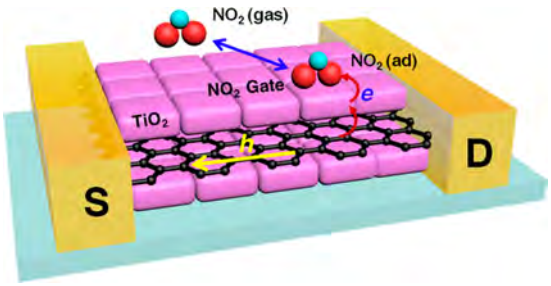

Figure 1. Schematic diagram of the rGO/TiO_2 heterojunction NO_2 field-effect sensor.

of the rGO films are homogeneously decorated with ultrasmall TiO_2 nanoparticles. This rGO/TiO_2 heterojunction provides us an excellent platform to rescrutinize the underlying sensing mechanisms of NO_2-gated nanosensors. In this configuration, NO_2 can immobilize free electrons in the decorated TiO_2 nanoparticles such that the NO_2-induced field effect can modulate the conductivity of the rGO underneath. There are two crucial factors in this design to be highlighted.

First, the selection of the rGO/TiO_2 system provides a relatively ideal model for studying gas-gated field-effect sensor. Explicitly, rGO, as a p-type material with high hole mobility (80−123 $cm^2\ V^{-1}\ s^{-1}$),[39] would dominate the overall electronic behavior of the device. Thus, due to its ultrathin thickness, the entire conductivity of rGO will be influenced by the electronic perturbations from the adsorbed gas molecule.[19] In addition, because TiO_2 generally possesses a lower intrinsic charge carrier concentration ($2.7 \times 10^{17}/cm^3$)[40] than SnO_2 ($3.6 \times 10^{18}/cm^3$)[41] (note: carrier concentrations of TiO_2 and SnO_2 depend largely on synthesis and crystal structures), TiO_2 would respond more "sensitively" to an external potential perturbation in comparison to SnO_2, since a certain number of adsorbed NO_2 molecules immobilize a greater percentage of the free electrons in TiO_2 than in SnO_2.

Second, the packing density of the decorated TiO_2 nanoparticles on rGO should be as high as possible to maximize the NO_2-induced charge separation that is the origin of the gate voltage on the rGO layer. Moreover, the decorated TiO_2 nanoparticle layer should be relatively uniform and thin (comparable to the width of gas-modulated space charge layer, typically 1−10 nm[23]) in order to form a uniform and effective electric field by gate voltage resulting from the adsorbed NO_2 molecules. Therefore, a monolayer of ultrathin TiO_2 nanoparticles packed densely on rGO is highly preferable to construct a simple but efficient model to study the underlying mechanisms of NO_2-gated field-effect sensor.

With all these aspects taken into consideration, our rGO/TiO_2 heterojunctions-based sensors exhibits a remarkable ppb-level sensitivity on NO_2 in the concentration range from 20 to 1000 ppb at 200 °C. The response time of the current NO_2 sensor ranges from 60 to 175 s depending on NO_2 concentrations. Furthermore, we show that an analytic model based on the integration of Van't Hoff equation, Graham function on surface charge density vs surface potential, and thin-film field-effect transistor theory can provide a quantitatively analysis on the corelation between the gas sorption thermodynamics and the measured source-drain current in this NO_2-gated field-effect nanosensor. Key thermodynamic parameters can be obtained from this model including adsorption equilibrium constant and adsorption enthalpy of NO_2 on TiO_2 nanoparticles.

■ EXPERIMENTAL SECTION

Preparation of GO. GO was synthesized chemically by oxidation of graphite using the modified Hummer's method. Briefly, 0.5 g of graphite powder (Bay Carbon, SP1), 0.55 g of sodium nitrate (Sigma-Aldrich, >99.999%), and 23 mL of sulfuric acid (Sigma-Aldrich, 99.999%) were mixed and stirred for 10 min. Then, 3 g of potassium permanganate (Sigma-Aldrich, >99.0%) was added slowly, and temperature was maintained below 20 °C. Deionized (DI) water was added slowly, and the temperature was raised to 90 °C. The solution turned bright yellow when 3 mL of hydrogen peroxide (30%) was added. The mixture was filtered while warm and washed with warm DI water. Purification was done by centrifugation. Graphite oxide (25 mg) was exfoliated in distilled water (7 mL) with 10 min of ultrasonic treatment to form a colloidal suspension.

Preparation of rGO/TiO_2 Heterojunction. 0.55 mL of $TiCl_4$ kept in a refrigerator was extracted using a 1 mL syringe and rapidly injected into the bottom of a parafilm sealed 100 mL bottle with 50 mL of DI water in the form of ice. After that, the bottle was firmly covered with the bottle cap and shaken continuously until the ice was dissolved. In the whole process, no white precipitation was observed. 1.12 mL of GO solution was injected into a 15 mL bottle with 10 mL of $TiCl_4$ solution and then kept stirring in a water bath at 50 °C for 72 h. The color of the solution turned from transparent to gray slowly. The precipitate was collected by centrifugation after being washed with deionized water and ethanol several times and then was dried completely at 70 °C. Finally, the products were kept in a ceramic crucible and annealed in a tubular oven at 500 °C for 30 min with nitrogen gas protection. The corresponding hybrid products were referred to as rGO/TiO_2 hetrojunctions.

Characterization of rGO/TiO_2. X-ray diffraction (XRD) measurement was carried out using powder XRD (Bruker D8 Advance, with Cu Kα radiation operating at 40 kV and 40 mA, scanning from 2θ = 10° to 90°). Field emission scanning electron microscopy (FESEM; JEOL JSM-7600F), transmission electron microscopy (JEOL 2100 TEM, 200 kV), Raman spectroscopy (LabRAM HR Evolution), and atomic force microscopy (AFM, MultiMode 8, BRUKER) were used to characterize the morphology of the samples. The Mott−Schottky (MS) plot was recorded by the electrochemical workstation (Zennium Workstation, ZAHNER, Germany), using the ac impedance method. The measurement was conducted in a conventional three-electrode cell, using a ceramic/Ag electrode with rGO/TiO_2 on the surface, a standard saturated Ag/AgCl, and a Pt wire as the working, reference, and counter electrodes, respectively. To measure the MS plot of rGO/TiO_2, the amplitude of the ac potential was set at 10 mV, the frequency was 1 kHz, and the electrolyte contained 0.1 M Na_2HPO_4 with solution pH adjusted to 10 (0.2 by 4 M NaOH).

Device Fabrication and Gas Sensing Testing. The as-synthesized sample was mixed with deionized water in a weight ratio of 100:25 and ground in a mortar for 15 min to form a paste. The paste was then coated on a ceramic substrate by a thin brush to form a sensing film on which silver interdigitated

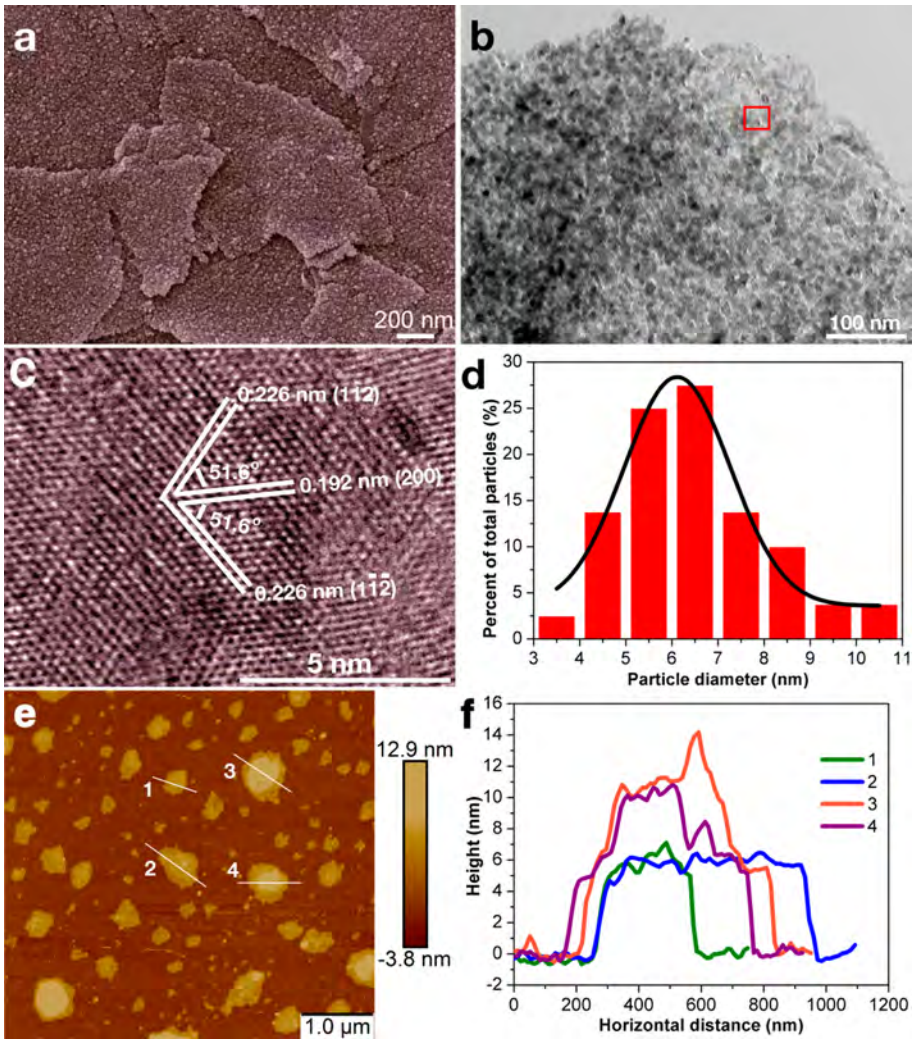

Figure 2. (a) FESEM, (b) TEM, and (c) HRTEM images of the rGO/TiO_2 heterojunction. (d) Size distribution of the decorated TiO_2 nanoparticles. (e) AFM image of the rGO/TiO_2 heterojunction dispersed on Si wafer. (f) Line profiling of four rGO/TiO_2 heterojunction sheets.

electrodes with both finger width and interfinger spacing of about 200 μm were previously printed. The sample was dried naturally in air overnight. Gas sensing properties were measured by a CGS-1TP (Chemical Gas Sensor-1 Temperature Pressure) intelligent gas sensing analysis system (Beijing Elite Tech Co., Ltd., China). The sensors were preheated at 200 °C for about 3 h. The required amount of gas was injected into the chamber (72 L) using a 1 mL syringe and was mixed with air (relative humidity was about 25%) by two fans in the analysis system. After the sensor resistances reached a new constant value, dry air was purged in to recover the sensor.

■ RESULTS AND DISCUSSION

Morphology Characterization of rGO/TiO_2 Hetrojunction Structure. For the first step, GO was synthesized chemically by oxidation of graphite using the modified Hummer's method and characterized by Raman and transmission electron microscope (TEM), as shown in Figures S1 and S2. It is clearly shown that GO was synthesized successfully. The rGO/TiO_2 heterojunctions were synthesized through a moderate *in situ* hydrothermal method at 50 °C using GO suspension and $TiCl_4$ solution as precursors, followed by an annealing at 500 °C for 30 min. The X-ray diffraction (XRD) pattern of the rGO/TiO_2 heterojunction structures before and after annealing confirmed that the majority of the as-grown nanoparticles are anatase TiO_2 (JCPDS, 21-1272), with only small amount of rutile TiO_2 (JCPDS, 01-1292) nanoparticles presented (Figure S3). It is shown that the annealing process could greatly improve the crystallinity of the structure. Field emission scanning electron microscopy (FESEM) image shows that ultrasmall TiO_2 nanoparticles were homogeneously grown on rGO sheet and closely packed with each other (Figure 2a). The nanogranular surface of the rGO/TiO_2 heterojunction is fairly homogeneous, and no aggregation of TiO_2 nanoparticles could be observed. To prove the existence of rGO in the rGO/TiO_2 heterojunction, the sample is characterized by Raman spectroscopy as depicted in Figure S4. The G-band and D-band remained unaltered compared to that of GO. The rGO/TiO_2 heterojunction shows a symmetric 2D and S3 band. The inset in Figure S4 shows a symmetric 2D-band of rGO/TiO_2 heterojunction at 2698 cm^{-1}, implying that rGO is present as a single layer graphene in the rGO/TiO_2 heterojunction.[42] Furthermore, TEM image in Figure 2b shows that TiO_2 nanoparticles were homogeneously and densely packed on rGO. Figure 2c shows the high resolution transmission electron microscopy (HRTEM) image of the rectangular region in Figure 2b. The lattice fringes along three directions (112), (200), and (1$\bar{1}$2) can be well identified

that are ascribed to anatase TiO_2. To statistically analyze the size of TiO_2 nanocrystals, a rectangular region in Figure 2b was further enlarged in Figure S5. The average size of the nanocrystals was obtained by counting the size of 80 nanocrystals and by Gauss fitting (Figure 2d). The average size of the TiO_2 nanocrystals was around 6 nm, which is in the width of the gas-modulated space charge layer, implying that a good interaction between NO_2, TiO_2, and rGO can be achieved.

To further check the morphology of the rGO/TiO_2 heterojunction, atomic force microscopy (AFM) study was conducted to measure the thickness of the heterojunction sheets (Figure 2e). From the line scan across different heterojunction sheets (Figure 2f), one can see that some of the heterojunction sheets are covered with one monolayer TiO_2 nanoparticle with height of ~6 nm (sheets 1 and 2). It is considered that the TiO_2 nanoparticles grow anisotropically on the surface of rGO since the sizes of them are around 6 nm and they grow on both surfaces of rGO. Some of the heterojunction sheets show a layer stacking behavior with a two-stair height profile from 6 to 12 nm (see sheets 3 and 4 as marked in Figure 2e). This is because that rGO/TiO_2 heterojunction sheets have a tendency to aggregate when they are dried due to $\pi-\pi$ stacking interactions between rGO sheets. A relatively uniform field effect would be induced due to the monolayer structure and the large conductance difference between TiO_2 and rGO when rGO/TiO_2 heterojunction acts as the sensing layer of a gas-gated field-effect sensor. As a result, this monolayer TiO_2 nanoparticles distribution on rGO is very desirable to study the sensing mechanisms of gas-gated field-effect sensor.

Gas Sensing Properties and Sensing Behavior. The rGO/TiO_2 heterojunction was fabricated into a NO_2-gated field-effect sensor (Figure S6 shows the top view and Figure S7 shows the cross section) and was characterized in various low-concentration NO_2 (20−1000 ppb) at elevated temperature, such as 200 °C using air as carrier gas. It should be noted that the sensor performance at room temperature is difficult to measure due to the limitation of the measurement instrument (maximum measuring resistance of 2 GΩ) and the large gap between the source and drain (200 μm, Figure S6). Figure 3a shows the typical dynamic responses of an rGO/TiO_2 device for detecting NO_2. Upon the injection of NO_2, the drain current (I_d) increases. Upon purging with clean air, the drain current of the device drops to the original level. This phenomenon can be repeated within the entire measurement range (20−1000 ppb), showing the excellent repeatability of the device.

To calibrate the sensor performance, the normalized sensor response (ratio of device drain current change to the initial drain current in air) as a function of NO_2 concentration (C) is plotted in Figure 3b. The responses of the sensor toward 20 and 1000 ppb NO_2 are 1.7% and 187%, respectively. One can see that the present NO_2 sensor response is much better than that of the corresponding TiO_2 nanoparticle or rGO NO_2 sensor (Figures S8 and S9). Furthermore, compared to the TiO_2 nanoparticle NO_2 sensor, the resistance is greatly reduced, and compared to the rGO NO_2 sensor, a pronounced recovery characteristic is shown. The curve can be well fitted with a quadratic equation (eq 1), and the coefficient of determination is 0.9979.

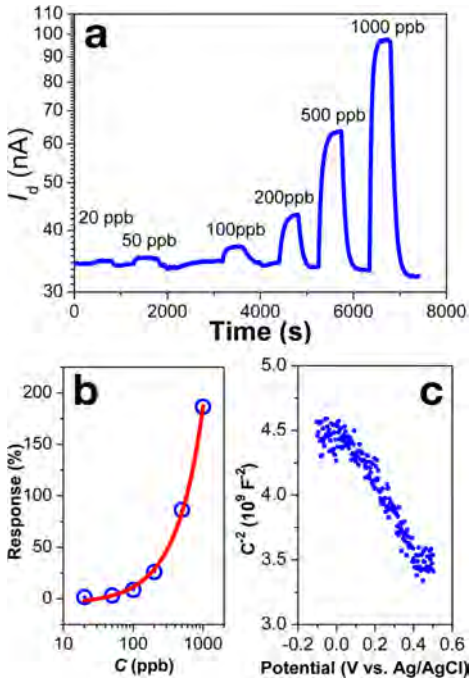

Figure 3. (a) Drain current (I_d) as a function of time when the rGO/TiO_2 heterojunction-based field-effect sensor was exposed to NO_2 with different concentrations. (b) Sensor response as a function of the concentration of NO_2. (c) Mott−Schottky plot of the rGO/TiO_2 heterojunction.

$$\text{response} = \frac{I_d - I_0}{I_0} \times 100\% = (-5.1 + 0.16C + 2.85 \times 10^{-5}C^2)\% \quad (1)$$

To further prove the reliability of the as-fabricated and calibrated rGO/TiO_2 NO_2 nanosensor, NO_2 with a concentration of 150 ppb was injected into the chamber three times. All three responses are between 18.5% and 21%, which are in good agreement with the fitted value of 19.1% (Figure S10), showing the repeatable responses and well-calibrated device performance. The response time (corresponds to the time it takes to cause 90% drain current change) of the sensor is between 80 and 175 s depending on the concentration of NO_2, and the recovery time is less than 220 s in the whole measuring range (Figure S11). These data show that the present rGO/TiO_2 sensor has a fast response toward ppb level NO_2 and can fully recover in a short period of time at 200 °C. The estimated limit of detection (defined as LOD = $3S_D/m$, where m is the slope of the linear part of the calibration curve (0.0016) and S_D is the standard deviation of noise (7.9×10^{-4}) in the response curve) of the rGO/TiO_2 NO_2 nanosensor is determined to be 1.5 ppb.

To further understand the sensing mechanisms of the current rGO/TiO_2 sensor, the semiconducting behavior of the rGO/TiO_2 heterojunction film was characterized by the Mott−Schottky (MS) plot according to the literature,[43] as shown in Figure 3c. The experiment was measured at the interface between rGO/TiO_2 in liquid electrolyte of Na_2HPO_4. The $1/C^2$ vs potential plot exhibits a negative slope, suggesting rGO/TiO_2 is p-type semiconducting, which is ascribed to the high electrical conductivity of rGO in the rGO/TiO_2 system. In contrast, the conductivity of TiO_2 is much lower than that of rGO at 200 °C; for example, the resistance value in air of the

pure electrospun TiO_2 nanofibers is around 20 GΩ,[23] and the resistance value of rGO is around 1 MΩ[21] and that for chemically modified graphene is around 100 MΩ.[44] Thus, the overall charge transport in rGO/TiO_2 nanosensors is dominated by the charge transport in the rGO layer. This can be confirmed by the sensing behavior comparison in dark condition and under UV light illumination at 150 °C when the rGO/TiO_2 heterojunction-based field-effect sensor was exposed to 100 ppb NO_2 gas, as shown in Figure S12. One can see that the drain current (I_d) increases once NO_2 gas was injected in dark condition (Figure S12a), indicating a p-type behavior. However, the drain current (I_d) decreases once NO_2 gas was injected under 367 nm UV light illumination (0.8 mW/cm^2) due to light absorption in TiO_2 (Figure S12b), indicating a n-type behavior. As a result, the sensor behavior can be dominated by the TiO_2 layer through light excitation. This result strongly confirmed that the present sensor behavior is p-type in dark condition. From Figure S12b, one can also get that there is charge redistribution in TiO_2 once NO_2 is adsorbed under light illumination condition.

Electrical Performance Modeling and Gas Adsorption Thermodynamics. The concept of field-effect nanosensor has been well established recently, such as in molecular gating of silicon nanowire FET with nonpolar analytes.[45] In the present study, the n-type TiO_2 ultrasmall nanoparticle layer undergoes a charge redistribution due to the high electron affinity of the surface adsorbed NO_2 gas, as schematically shown in Figure 1. Consequently, a negative gate voltage can be established in the proximity of the rGO layer that leads to the drain current increase in the p-type rGO.[19,44] The drain current (I_d) characteristics of an rGO/TiO_2 nanosensor under different concentrations of NO_2 are shown in Figure S13. It is clearly shown that with the increase of the NO_2 concentration I_d increases, indicating a negative voltage gated field effect induced by NO_2 gas. To quantitatively correlate the gas adsorption thermodynamics and the drain current, the analytic model of field-effect transistor is first illustrated as follows.

In a typical metal−insulator−semiconductor field-effect transistor (MISFET), the drain current in the saturation regime is given by eq 2

$$I_d = \frac{W}{2L}\mu C_i(V_g - V_t)^2 \tag{2}$$

where W is the channel width, L is the channel length, μ is the charge mobility, C_i is the insulator (TiO_2 nanoparticle) capacitance (per unit area), V_g is the source-gate voltage, and V_t is the threshold voltage. In a field-effect gas sensor, V_g is provided by the surface potential (ψ).[46] ψ is related to the surface charge density (σ), and the relationship between ψ and σ can be calculated by using the Grahame equation (eq 3)[47]

$$\sigma = \sqrt{8\varepsilon\varepsilon_0 kTc_0}\,\sinh\left(\frac{e\Psi}{2kT}\right) \tag{3}$$

where k is the Boltzmann constant, T is absolute temperature, e is elementary charge, ε_0 is the permittivity of free space, ε is the dielectric constant of TiO_2, and c_0 is the buffer ionic strength. In our case, TiO_2 nanoparticles could be considered as the buffer. According to the definition of ionic strength, c_0 equals to $e^2n_d/2$, where n_d is the carrier concentration in TiO_2.[48]

Since the concentration of NO_2 gas is in ppb level, the surface potential changes induced by the adsorbed gas molecules is very little; as a result, the Grahame equation could be simplified as eq 4 (a detailed derivation is shown in the Supporting Information)

$$\sigma = \varepsilon\varepsilon_0 e\Psi\frac{1}{L_D} \tag{4}$$

where L_D is the Debye length[49] and is defined as eq 5

$$L_D = \sqrt{\frac{\varepsilon\varepsilon_0 kT}{e^2 n_d}} = A\sqrt{T} \tag{5}$$

where A is a constant. It is assumed that the surface charge density is proportional to the concentration of the surface-adsorbed NO_2 molecules, denoted as $[NO_2]_s$,[47] and can be typically expressed as eq 6

$$\sigma = g[NO_2]_s \tag{6}$$

where g is a constant and $[NO_2]_s$ is the concentration of the adsorbed NO_2 molecules on the surface of the sensing material. According to the definition of equilibrium constant (eq 7)

$$K = \frac{[NO_2]_s}{C} \tag{7}$$

where C is the concentration of NO_2 in bulk gas phase. Thus, by combining eqs 2, 4, 6, and 7, the relationship between drain current and the concentration of gas phase NO_2 could be deduced as eq 8.

$$I_d = \frac{W}{2L}\mu C_i\left(\frac{gL_D}{\varepsilon\varepsilon_0 e}KC - V_t\right)^2 \tag{8}$$

Equation 8 can be normalized by the initial drain current (I_0), as shown in eq 9.

$$\frac{I_d}{I_0} = \left(\frac{gL_D}{\varepsilon\varepsilon_0 e}\frac{1}{V_t}KC - 1\right)^2 \tag{9}$$

When the concentration of NO_2 gas is very high, such as at the ppm level, eq 3 could not be simplified as eq 4, as detailed derived in the Supporting Information. This is evidenced by the sensing performance of an independent ppm level NO_2-gated rGO/TiO_2 heterojunction field-effect sensor (Figure S14a,b). It is shown that there is a saturation phenomenon with the increase of the concentration of NO_2. In this condition, there is a quadratic relationship between I_d/I_0 and ln C, as shown in Figure S14c.

In the present study, the rGO/TiO_2-based NO_2 field-effect sensors are tested toward NO_2 under different concentrations at 150, 180, 200, and 220 °C, as shown in Figure S15. The relationship between I_d/I_0 and the concentration of NO_2 at different temperatures is shown in Figure 4a and can be well fit with quadratic equations (Table S1). The importance of the quadratic term is further confirmed in Table S2. As a result, the square root of I_d/I_0 has a linear relationship versus the concentration of NO_2, as expressed by eq 10. The details of the linear fitting are shown in Figure S16 and Table S3.

$$\sqrt{\frac{I_d}{I_0}} = \left|\frac{gL_D}{\varepsilon\varepsilon_0 e}\frac{1}{V_t}KC - 1\right| \tag{10}$$

According to the indefinite integral form of Van't Hoff equation (eq 11)[50,51]

$$\ln K = -\frac{\Delta H}{R}\frac{1}{T} + c' \tag{11}$$

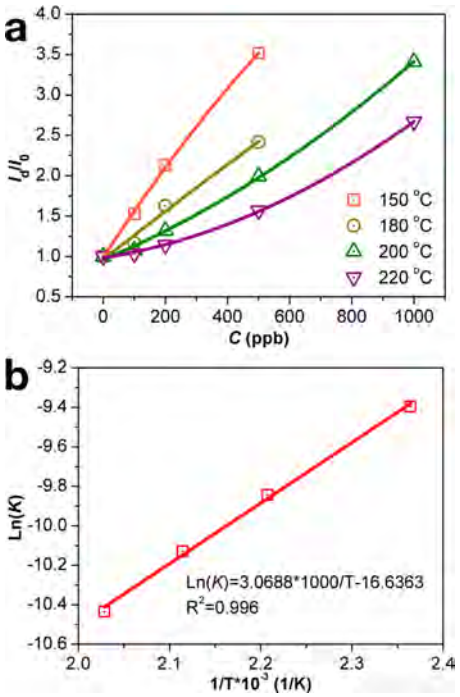

Figure 4. (a) I_d/I_0 versus concentration of NO_2 (C) at 150, 180, 200, and 220 °C and (b) logarithmic value of the NO_2 adsorption equilibrium constant (ln K) vs $1/T$.

where ΔH is standard molar enthalpy of adsorption, R is ideal gas constant, and c' is a constant, the equilibrium constant K can be expressed as eq 12

$$K = B \exp\left(-\frac{\Delta H}{R}\frac{1}{T}\right) \tag{12}$$

where B is a constant. By combining eqs 5, 10, and 12, the relationship between $(I_d/I_0)^{1/2}$, ΔH, T, and C could be expressed as eq 10-a

$$\sqrt{\frac{I_d}{I_0}} = \left|\frac{gAB}{\varepsilon\varepsilon_0 e}\frac{1}{V_t}\sqrt{T}\exp\left(-\frac{\Delta H}{R}\frac{1}{T}\right)C - 1\right| = \left|b\sqrt{T}\exp\left(-\frac{\Delta H}{R}\frac{1}{T}\right)C - 1\right| \tag{10-a}$$

where b is a constant. As a result, the relationship between the logarithmic value of $bT^{1/2}\exp(-\Delta H/(RT))$ and the equilibrium constant K can be obtained eq 13

$$\ln\left(b\sqrt{T}\exp\left(-\frac{\Delta H}{R}\frac{1}{T}\right)\right) - \frac{\ln T}{2} = \ln|b| - \frac{\Delta H}{R}\frac{1}{T} = \ln K \tag{13}$$

The logarithmic value of the equilibrium constant (ln K) versus $1/T$ is shown in Figure 4b. The standard molar enthalpy of adsorption is calculated to be −25.51 kJ/mol or 0.265 eV, which is in excellent agreement with the reported value (−23.56 kJ/mol).[52] This value indicates chemisorptions of NO_2 on TiO_2, likely in the surface defective sites such as oxygen vacancy. The absolute value of constant b can also be obtained and the value is 5.956×10^{-8}. Thus, eq 10-a can be transformed to eq 10-b

$$\sqrt{\frac{I_d}{I_0}} = 5.956 \times 10^{-8}\sqrt{T}\exp\left(3068.8\frac{1}{T}\right)C + 1 \tag{10-b}$$

where the unit of C is ppb.

To evaluate the accuracy of eq 10-b, an independently measured $(I_d/I_0)^{1/2}$ at 200 °C of the rGO/TiO_2-based NO_2 field-effect sensor (data shown in Figure 3a) was used to compare with the calculated $(I_d/I_0)^{1/2}$ at 200 °C according to eq 10-b, as shown in Figure 5. The difference between the measured values and the calculated values are less than 4.5% when the concentration of NO_2 is below 500 ppb and only slightly increases to 8.6% as the NO_2 concentration increases to 1000 ppb. This result manifests a good agreement between the theoretical predicted sensor signals and the experimental values.

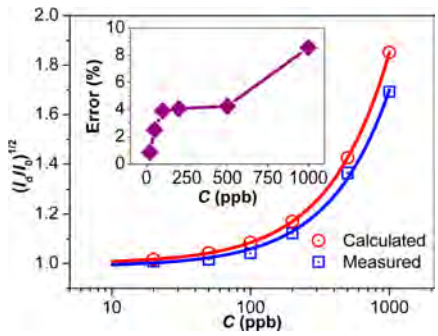

Figure 5. Comparison of the measured $(I_d/I_0)^{1/2}$ at 200 °C of an independent measurement of the rGO/TiO_2-based NO_2 field-effect sensor (blue) and the calculated $(I_d/I_0)^{1/2}$ at 200 °C (red); the inset is the error between the measured value and the calculated value.

According to eq 10-a, there is an exponential relation between the sensor sensitivity and ΔH, and this relation has been well confirmed by the sensitivities of metallophthalocyanine chemiresistors to vapor phase electron donors.[50] An analyte with a high binding enthalpy would lead to a strong sensor response, which exponentially depends on ΔH.[50] Thus, it is suggested to compare ΔH in different systems first in order to optimize the sensing materials (such as the morphology, the exposed facets). If the standard molar enthalpy of adsorption of a system (determined by both the sensing material and the target gas) is obtained, the sensor signal $(I_d/I_0)^{1/2}$ should be solely determined by the operating temperature of the device and the concentration of the target gas. With the increase of the temperature, the sensor signal decreases. As a result, the sensitivity of a gas-modulated field-effect sensor can be theoretically predicted in our analytical model. However, to compare the sensor signal from device to device, the contribution from the threshold voltage should also be considered.

From eqs 4, 6, and 7 and the calculated standard molar enthalpy of adsorption, the equilavent gate voltage induced by different concentrations of NO_2 at a working temperature of 200 °C can also be approximately estimated, as shown in Part 4 of the Supporting Information. The gate voltage values versus NO_2 concentrations is shown in Figure S17. At a NO_2 concentration of 100 ppb, the equivalent gate voltage value is 4.712 mV, and at a NO_2 concentration of 1000 ppb, the equivalent gate voltage value is 47.12 mV.

■ CONCLUSIONS

A NO_2-gated rGO/TiO_2 heterojunction field-effect NO_2 sensor was fabricated to understand the underlying sensing mechanisms of nanomaterial-based electrical gas sensors. The drain currents at different temperatures under 20−1000 ppb NO_2

were tested and fitted with quadratic equations. The standard molar enthalpy of adsorption of the present sensing system was obtained to be −25.51 kJ/mol. A quantitative relation between the sensor signal, the concentration of the target gas, and the operating temperature was established. The obtained formula can describe well the response characteristics of the NO_2-gated rGO/TiO_2 heterojunction field-effect sensor. In perspective, this work provides the fundamental understanding of the underlying physics and chemistry for designing high-performance gas-modulated field-effect sensor. Particularly, the capability of acquiring the gas adsorption enthalpy via this model provides an alternative way for developing nonspecific gas sensors that can identify the nature of various adsorbed molecules because the adsorption enthalpy is highly molecule dependent.

■ ASSOCIATED CONTENT

Ⓢ Supporting Information

Additional figures and modeling details. This material is available free of charge via the Internet at http://pubs.acs.org.

■ AUTHOR INFORMATION

Corresponding Authors

*E-mail xcdou@ms.xjb.ac.cn (X.D.).
*E-mail txu@niu.edu (T.X.).

Author Contributions

B.Z., B.L., and Z.Y. contributed equally.

Notes

The authors declare no competing financial interest.

■ ACKNOWLEDGMENTS

We thank the financial support from the West Light Foundation of the Chinese Academy of Sciences (LHXZ201102), Xinjiang International Science & Technology Cooperation Program (20136008), the Xinjiang Program of Cultivation of Young Innovative Technical Talents (2013711015), National Natural Science Foundation of China (51372273), "Hundred Talents Program" of the Chinese Academy of Sciences, and the SRF for ROCS, SEM. T.X. also acknowledges the support from the US National Science Foundation (CBET-1150617).

■ REFERENCES

(1) Cui, Y.; Wei, Q.; Park, H.; Lieber, C. M. Nanowire Nanosensors for Highly Sensitive and Selective Detection of Biological and Chemical Species. *Science* **2001**, *293*, 1289−1292.

(2) Swierczewska, M.; Liu, G.; Lee, S.; Chen, X. High-Sensitivity Nanosensors for Biomarker Detection. *Chem. Soc. Rev.* **2012**, *41*, 2641−2655.

(3) Kemling, J. W.; Qavi, A. J.; Bailey, R. C.; Suslick, K. S. Nanostructured Substrates for Optical Sensing. *J. Phys. Chem. Lett.* **2011**, *2*, 2934−2944.

(4) Gao, A.; Lu, N.; Wang, Y.; Dai, P.; Li, T.; Gao, X.; Wang, Y.; Fan, C. Enhanced Sensing of Nucleic Acids with Silicon Nanowire Field Effect Transistor Biosensors. *Nano Lett.* **2012**, *12*, 5262−5268.

(5) Nguyen, P.; Berry, V. Graphene Interfaced with Biological Cells: Opportunities and Challenges. *J. Phys. Chem. Lett.* **2012**, *3*, 1024−1029.

(6) Wang, C.; Summers, C. J.; Wang, Z. L. Large-Scale Hexagonal-Patterned Growth of Aligned ZnO Nanorods for Nano-optoelectronics and Nanosensor Arrays. *Nano Lett.* **2004**, *4*, 423−426.

(7) Yu, K.; Lu, G.; Bo, Z.; Mao, S.; Chen, J. Carbon Nanotube with Chemically Bonded Graphene Leaves for Electronic and Optoelectronic Applications. *J. Phys. Chem. Lett.* **2011**, *2*, 1556−1562.

(8) Aguilar, A. D.; Forzani, E. S.; Leright, M.; Tsow, F.; Cagan, A.; Iglesias, R. A.; Nagahara, L. A.; Amlani, I.; Tsui, R.; Tao, N. J. A Hybrid Nanosensor for TNT Vapor Detection. *Nano Lett.* **2009**, *10*, 380−384.

(9) Star, A.; Joshi, V.; Skarupo, S.; Thomas, D.; Gabriel, J.-C. P. Gas Sensor Array Based on Metal-Decorated Carbon Nanotubes. *J. Phys. Chem. B* **2006**, *110*, 21014−21020.

(10) Al-Mashat, L.; Shin, K.; Kalantar-zadeh, K.; Plessis, J. D.; Han, S. H.; Kojima, R. W.; Kaner, R. B.; Li, D.; Gou, X.; Ippolito, S. J.; et al. Graphene/Polyaniline Nanocomposite for Hydrogen Sensing. *J. Phys. Chem. C* **2010**, *114*, 16168−16173.

(11) Robinson, J. T.; Perkins, F. K.; Snow, E. S.; Wei, Z.; Sheehan, P. E. Reduced Graphene Oxide Molecular Sensors. *Nano Lett.* **2008**, *8*, 3137−3140.

(12) Zeng, X. Q.; Latimer, M. L.; Xiao, Z. L.; Panuganti, S.; Welp, U.; Kwok, W. K.; Xu, T. Hydrogen Gas Sensing with Networks of Ultrasmall Palladium Nanowires Formed on Filtration Membranes. *Nano Lett.* **2010**, *11*, 262−268.

(13) Zeng, X. Q.; Wang, Y. L.; Deng, H.; Latimer, M. L.; Xiao, Z. L.; Pearson, J.; Xu, T.; Wang, H. H.; Welp, U.; Crabtree, G. W.; et al. Networks of Ultrasmall Pd/Cr Nanowires as High Performance Hydrogen Sensors. *ACS Nano* **2011**, *5*, 7443−7452.

(14) Tjoa, V.; Jun, W.; Dravid, V.; Mhaisalkar, S.; Mathews, N. Hybrid Graphene-Metal Nanoparticle Systems: Electronic Properties and Gas Interaction. *J. Mater. Chem.* **2011**, *21*, 15593−15599.

(15) Pan, X.; Liu, X.; Bermak, A.; Fan, Z. Self-Gating Effect Induced Large Performance Improvement of ZnO Nanocomb Gas Sensors. *ACS Nano* **2013**, *7*, 9318−9324.

(16) Cui, S.; Wen, Z.; Mattson, E. C.; Mao, S.; Chang, J.; Weinert, M.; Hirschmugl, C. J.; Gajdardziska-Josifovska, M.; Chen, J. Indium-Doped SnO_2 Nanoparticle-Graphene Nanohybrids: Simple One-Pot Synthesis and their Selective Detection of NO_2. *J. Mater. Chem. A* **2013**, *1*, 4462−4467.

(17) Samet, J. M. Traffic, Air Pollution, and Health. *Inhalation Toxicol.* **2007**, *19*, 1021−1027.

(18) Brunekreef, B.; Holgate, S. Air Pollution and Health. *Lancet* **2002**, *360*, 1233−42.

(19) Mao, S.; Cui, S.; Lu, G.; Yu, K.; Wen, Z.; Chen, J. Tuning Gas-Sensing Properties of Reduced Graphene Oxide Using Tin Oxide Nanocrystals. *J. Mater. Chem.* **2012**, *22*, 11009−11013.

(20) Lu, G.; Park, S.; Yu, K.; Ruoff, R. S.; Ocola, L. E.; Rosenmann, D.; Chen, J. Toward Practical Gas Sensing with Highly Reduced Graphene Oxide: A New Signal Processing Method To Circumvent Run-to-Run and Device-to-Device Variations. *ACS Nano* **2011**, *5*, 1154−1164.

(21) Lu, G.; Ocola, L. E.; Chen, J. Reduced Graphene Oxide for Room-Temperature Gas Sensors. *Nanotechnology* **2009**, *20*, 445502.

(22) Yavari, F.; Chen, Z.; Thomas, A. V.; Ren, W.; Cheng, H.-M.; Koratkar, N. High Sensitivity Gas Detection Using a Macroscopic Three-Dimensional Graphene Foam Network. *Sci. Rep.* **2011**, *1*, 166−5.

(23) Kim, I.-D.; Rothschild, A.; Lee, B. H.; Kim, D. Y.; Jo, S. M.; Tuller, H. L. Ultrasensitive Chemiresistors Based on Electrospun TiO_2 Nanofibers. *Nano Lett.* **2006**, *6*, 2009−2013.

(24) Shubhda, S.; Kiran, J.; Singh, V. N.; Sukhvir, S.; Vijayan, N.; Nita, D.; Govind, G.; Senguttuvan, T. D. Faster Response of NO_2 Sensing in Graphene−WO_3 Nanocomposites. *Nanotechnology* **2012**, *23*, 205501.

(25) Yang, Z.; Guo, L. J.; Zu, B. Y.; Guo, Y. N.; Xu, T.; Dou, X. C. CdS/ZnO Core/Shell Nanowire-Built Films for Enhanced Photodetecting and Optoelectronic Gas-Sensing Applications. *Adv. Opt. Mater.* **2014**, DOI: 10.1002/adom.201400086.

(26) Song, X.; Hu, J.; Zeng, H. Two-Dimensional Semiconductors: Recent Progress and Future Perspectives. *J. Mater. Chem. C* **2013**, *1*, 2952−2969.

(27) Kumar, M. K.; Ramaprabhu, S. Nanostructured Pt Functionlized Multiwalled Carbon Nanotube Based Hydrogen Sensor. *J. Phys. Chem. B* **2006**, *110*, 11291−11298.

(28) Joshi, R. K.; Gomez, H.; Alvi, F.; Kumar, A. Graphene Films and Ribbons for Sensing of O_2, and 100 ppm of CO and NO_2 in Practical Conditions. *J. Phys. Chem. C* **2010**, *114*, 6610−6613.
(29) Zhang, M.; Su, H. C.; Rheem, Y.; Hangarter, C. M.; Myung, N. V. A Rapid Room-Temperature NO_2 Sensor Based on Tellurium−SWNT Hybrid Nanostructures. *J. Phys. Chem. C* **2012**, *116*, 20067−20074.
(30) Yavari, F.; Koratkar, N. Graphene-Based Chemical Sensors. *J. Phys. Chem. Lett.* **2012**, *3*, 1746−1753.
(31) Zhang, J. Z. Improved Sensing with Nanostructures. *J. Phys. Chem. Lett.* **2012**, *3*, 1806−1807.
(32) Cui, S.; Mao, S.; Lu, G.; Chen, J. Graphene Coupled with Nanocrystals: Opportunities and Challenges for Energy and Sensing Applications. *J. Phys. Chem. Lett.* **2013**, *4*, 2441−2454.
(33) Paul, R. K.; Badhulika, S.; Saucedo, N. M.; Mulchandani, A. Graphene Nanomesh as Highly Sensitive Chemiresistor Gas Sensor. *Anal. Chem.* **2012**, *84*, 8171−8178.
(34) Kamat, P. V. Graphene - A Physical Chemistry Perspective. *J. Phys. Chem. Lett.* **2010**, *1*, 587−588.
(35) Williams, G.; Seger, B.; Kamat, P. V. TiO_2-Graphene Nanocomposites. UV-Assisted Photocatalytic Reduction of Graphene Oxide. *ACS Nano* **2008**, *2*, 1487−1491.
(36) Muszynski, R.; Seger, B.; Kamat, P. V. Decorating Graphene Sheets with Gold Nanoparticles. *J. Phys. Chem. C* **2008**, *112*, 5263−5266.
(37) Kamat, P. V. Graphene-Based Nanoarchitectures. Anchoring Semiconductor and Metal Nanoparticles on a Two-Dimensional Carbon Support. *J. Phys. Chem. Lett.* **2009**, *1*, 520−527.
(38) Lightcap, I. V.; Kosel, T. H.; Kamat, P. V. Anchoring Semiconductor and Metal Nanoparticles on a Two-Dimensional Catalyst Mat. Storing and Shuttling Electrons with Reduced Graphene Oxide. *Nano Lett.* **2010**, *10*, 577−583.
(39) Feng, H.; Cheng, R.; Zhao, X.; Duan, X.; Li, J. A Low-Temperature Method to Produce Highly Reduced Graphene Oxide. *Nat. Commun.* **2013**, *4*, 1539.
(40) Hwang, Y. J.; Boukai, A.; Yang, P. High Density n-Si/n-TiO_2 Core/Shell Nanowire Arrays with Enhanced Photoactivity. *Nano Lett.* **2008**, *9*, 410−415.
(41) Ogawa, H.; Nishikawa, M.; Abe, A. Hall Measurement Studies and an Electrical Conduction Model of Tin Oxide Ultrafine Particle Films. *J. Appl. Phys.* **1982**, *53*, 4448−4455.
(42) Sher Shah, M. S. A.; Park, A. R.; Zhang, K.; Park, J. H.; Yoo, P. J. Green Synthesis of Biphasic TiO_2-Reduced Graphene Oxide Nanocomposites with Highly Enhanced Photocatalytic Activity. *ACS Appl. Mater. Interfaces* **2012**, *4*, 3893−3901.
(43) Wu, S.; Yin, Z.; He, Q.; Huang, X.; Zhou, X.; Zhang, H. Electrochemical Deposition of Semiconductor Oxides on Reduced Graphene Oxide-Based Flexible, Transparent, and Conductive Electrodes. *J. Phys. Chem. C* **2010**, *114*, 11816−11821.
(44) Yuan, W.; Liu, A.; Huang, L.; Li, C.; Shi, G. High-Performance NO_2 Sensors Based on Chemically Modified Graphene. *Adv. Mater.* **2013**, *25*, 766−771.
(45) Paska, Y.; Stelzner, T.; Assad, O.; Tisch, U.; Christiansen, S.; Haick, H. Molecular Gating of Silicon Nanowire Field-Effect Transistors with Nonpolar Analytes. *ACS Nano* **2011**, *6*, 335−345.
(46) Bourguiga, R.; Garnier, F.; Horowitz, G.; Hajlaoui, R.; Delannoy, P.; Hajlaoui, M.; Bouchriha, H. Simulation of I-V Characteristics of Organic Thin Film Transistor: Application to the Dihexylquaterthiophene. *Eur. Phys. J. AP* **2001**, *14*, 121−125.
(47) Fritz, J.; Cooper, E. B.; Gaudet, S.; Sorger, P. K.; Manalis, S. R. Electronic Detection of DNA by its Intrinsic Molecular Charge. *Proc. Natl. Acad. Sci. U. S. A.* **2002**, *99*, 14142−14146.
(48) Solomon, T. The Definition and Unit of Ionic Strength. *J. Chem. Educ.* **2001**, *78*, 1691.
(49) Franke, M. E.; Koplin, T. J.; Simon, U. Metal and Metal Oxide Nanoparticles in Chemiresistors: Does the Nanoscale Matter? *Small* **2006**, *2*, 36−50.
(50) Bohrer, F. I.; Colesniuc, C. N.; Park, J.; Ruidiaz, M. E.; Schuller, I. K.; Kummel, A. C.; Trogler, W. C. Comparative Gas Sensing in Cobalt, Nickel, Copper, Zinc, and Metal-Free Phthalocyanine Chemiresistors. *J. Am. Chem. Soc.* **2008**, *131*, 478−485.
(51) Holmstrom, E. D.; Nesbitt, D. J. Real-Time Infrared Overtone Laser Control of Temperature in Picoliter H_2O Samples: "Nano-bathtubs" for Single Molecule Microscopy. *J. Phys. Chem. Lett.* **2010**, *1*, 2264−2268.
(52) Wanbayor, R.; Ruangpornvisuti, V. Adsorption of Di-, Tri- and Polyatomic Gases on the Anatase TiO_2 (001) and (101) Surfaces and their Adsorption Abilities. *J. Mol. Struct.: THEOCHEM* **2010**, *952*, 103−108.